

Microfabricated High-Speed Axial-Flux Multiwatt Permanent-Magnet Generators—Part II: Design, Fabrication, and Testing

David P. Arnold, *Member, IEEE*, Sauparna Das, *Member, IEEE*, Jin-Woo Park, Iulica Zana, *Member, IEEE*, Jeffrey H. Lang, *Fellow, IEEE*, and Mark G. Allen, *Senior Member, IEEE*

Abstract—This paper presents the design, fabrication, and characterization of permanent-magnet (PM) generators for use in microscale power generation systems. The generators are three-phase, axial-flux, synchronous machines, each consisting of an eight-pole surface-wound stator and PM rotor. The devices are fabricated using a combination of microfabrication and precision assembly. Characterization is achieved using a custom-built experimental test stand that incorporates an off-the-shelf gas-driven spindle to power the machines. At a rotational speed of 120 000 rpm, one generator demonstrates 2.5 W of mechanical-to-electrical power conversion and, coupled to a transformer and rectifier, delivers 1.1 W of dc electrical power to a resistive load. This watt-scale electrical power generation demonstrates the viability of scaled PM machines for practical power generation applications. [1701]

Index Terms—AC generators, micromachining, permanent-magnet (PM) machines, power microelectromechanical systems (MEMS).

I. INTRODUCTION

MINIATURIZED permanent-magnet (PM) synchronous machines show promise for high-density power conversion in portable electronics, robotics, and various other microsystem applications. Axial-flux rotating machines are of particular interest to the MEMS community because wafer-level processes are readily available for fabricating structures with

Manuscript received October 15, 2005; revised May 1, 2006. This work was supported in part by the U.S. Army Research Laboratory under the Collaborative Technology Alliance Program (DAAD19-01-2-0010). This work was presented in part at the 18th IEEE International Conference on Micro Electro Mechanical Systems, Miami Beach, FL, January 2005. Subject Editor D.-I. Cho.

D. P. Arnold was with the Georgia Institute of Technology, Atlanta, GA 30332-0269 USA. He is now with the Department of Electrical and Computer Engineering, University of Florida, Gainesville, FL 32611-6200 USA (e-mail: darnold@ufl.edu).

S. Das was with the Massachusetts Institute of Technology, Cambridge, MA 02139-4307 USA. He is now with Linear Technology, North Chelmsford, MA 01863 USA (e-mail: sdas@linear.com).

J.-W. Park was with the Georgia Institute of Technology, Atlanta, GA 30332-0269 USA. He is now with CardioMEMS, Inc., Atlanta, GA 30308 USA (e-mail: jp190@mail.gatech.edu).

I. Zana was with the Georgia Institute of Technology, Atlanta, GA 30332-0269 USA. He is now with the Center for Materials for Information Technology, University of Alabama, Tuscaloosa, AL 35487 USA (e-mail: izana@mint.ua.edu).

J. H. Lang is with the Department of Electrical Engineering and Computer Science, Massachusetts Institute of Technology, Cambridge, MA 02139-4307 USA (e-mail: lang@mit.edu).

M. G. Allen is with the School of Electrical and Computer Engineering, Georgia Institute of Technology, Atlanta, GA 30332-0269 USA (e-mail: mark.allen@ece.gatech.edu).

Digital Object Identifier 10.1109/JMEMS.2006.880286

the requisite planar geometries. Microfabrication offers several design advantages for miniaturization over conventional machine manufacturing technologies involving stamped parts and wound windings. First, the windings can be photolithographically defined, which permits optimized winding patterns with variable-width conductors. Second, high-resolution features can help reduce certain losses; skin effects can be reduced by using windings with small cross sections and eddy current losses in the magnetic core can be reduced by using laminations of micron scale thicknesses. Third, intimate thermal contact of electroplated windings to their substrate greatly enhances heat transfer and allows for substantially increased current density. Finally, batch fabrication offers the opportunity for high-volume, low-cost production.

Microfabricated PM axial-flux machines have been previously demonstrated as both motors [1]–[3] and generators [4], [5]. In both cases, the machines consist of two key components: a rotor with a multipoled PM and a stator with appropriately designed windings. In most cases, the stator windings were formed using multilayer copper electrodeposition on a substrate of silicon or ferrite. The rotors were formed either with discrete magnets [2], [4] or by impressing a magnetic pole pattern on a disc-like annulus [1], [3], [5]. SmCo [2], [5] or NdFeB [2]–[4] were typically used for the PM material. Peripheral design modifications, such as optimized winding patterns, inclusion of soft magnetic materials [1], [3], [4], and dual stators [2], [4], have been explored in order to maximize the electromechanical power conversion. Also, various methods, ranging from simple shafts [1], [3], [4] to magnetic bearings [2], [5] and air bearings [5] have been used to stabilize the spinning rotor over the surface of the stator.

This paper follows the modeling efforts of [6] and focuses on the fabrication and characterization of PM generators capable of spinning at high speeds (100 000+rpm) and generating watt-level power. First, an overview of the machine is presented, followed by the microfabrication and precision conventional machining used for fabrication. Next, a spinning rotor test stand, using an air-powered spindle for rotational testing, is described. Finally, the device characterization, including electrical measurements of the stators, open-circuit voltages, and dc power delivered to a resistive load using passive power electronics, is discussed, and comparisons with the theoretical models are made.

II. GENERATOR DESIGN

The generators are three-phase, eight-pole, axial-flux, synchronous machines, as shown in Fig. 1. Each comprises a rotor

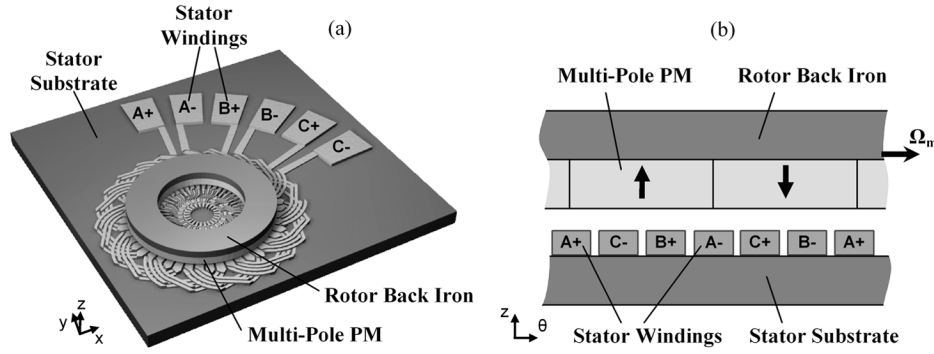


Fig. 1. Conceptual drawing of the PM generator: (a) perspective view and (b) cross section.

with an annular PM and soft magnetic back iron and a stator with multturn surface windings on a soft magnetic substrate (back iron). In operation, rotation of the multipoled magnetic rotor creates time-varying magnetic fields, which induce voltages on the stator windings, as governed by Faraday's Law [7]. The PM provides a permanent magnetic field source, and the soft magnetic substrate and rotor back iron reduce the magnetic reluctance in order to maximize the magnetic flux for greater power density.

The simplified equivalent circuit equations from [6] can be used to derive some analytical insight into how to best design the generator for maximum power density. As given by [6, eq. (101)], the single-phase open-circuit voltage V_{oc} is proportional to several design parameters

$$V_{oc} \propto \left(\frac{T_{al}}{T_{al} + T_{cl} + T_{ag}} B_r \right) PN\Omega_m \quad (1)$$

where T_{al} , T_{cl} , and T_{ag} , are the thicknesses of the PM, the coil layer, and the air gap, respectively, B_r is the PM remanence, P is the number of poles, N is the number of turns/pole, and Ω_m is the angular velocity. The open circuit voltage is seen to be proportional to P , N , B_r , and the machine speed Ω_m . The single-phase resistance

$$R_s \propto \frac{(PN)^2}{T_{cl}} \quad (2)$$

as given by [6, eq. (111)] is proportional to the square of P and N and inversely proportional to the thickness of the coil layer T_{cl} . Thus, the scaling of the output power of a PM generator can be approximated by

$$P_{out} \propto \frac{V_{oc}^2}{R_s} \propto \left(\Omega_m B_r \frac{T_{al} \sqrt{T_{cl}}}{T_{al} + T_{ag} + T_{cl}} \right)^2 \quad (3)$$

Equation (3) indicates that, to first order, the machine output power is independent of P or N but scales quadratically with both speed and PM remanence. The fraction yields important information about the relative thicknesses of the permanent magnet (T_{al}), coil layer (T_{cl}), and air gap (T_{ag}) in order to maximize output power. First, the air gap should be made as small as possible, but fabrication tolerances, rotor stability, and the need to limit viscous losses (windage) all play a role

in determining the minimum gap (i.e., the gap is fixed by a combination of system-level tradeoffs). Second, it can be shown that the fraction in (3) is maximized when

$$T_{cl} = T_{al} + T_{ag}. \quad (4)$$

Thus, the thickness of the coil layer should be designed to be the sum of the thickness of the magnet and air gap.

In the design of the machine under investigation in this paper, the thickness of the PM is fixed at $500 \mu\text{m}$ by microengine constraints, and the minimum air gap used is $100 \mu\text{m}$. According to (4) the coil layer should be $600 \mu\text{m}$ for maximum power. However, the maximum height of the coil layer is $\sim 200 \mu\text{m}$ due to limitations of the photolithography used to fabricate the coils. Therefore, given the design constraints, the coil layer is designed for the maximum value of $200 \mu\text{m}$.

A. Rotor Design

The rotor contains an eight-pole, annular, pressure-formed (sintered) $\text{Sm}_2\text{Co}_{17}$ PM and a ferromagnetic $\text{Fe}_{49}\text{Co}_{49}\text{V}_2$ (Hiperco50) back iron, as shown in Fig. 2. The PM and rotor back iron are $500 \mu\text{m}$ thick and have an outer diameter (OD) of 9.525 mm and inner diameter (ID) of 3.175 mm . The rotor components are mounted in a poly(methyl methacrylate) (PMMA) adaptor for assembly onto a 1.6-mm diameter shaft for testing. Note that the rotor components have a smaller ID than the stator; this is because magnets of these dimensions were commercially available in small quantities, without the need for custom (and costly) manufacturing.

SmCo was selected for its combination of high energy product ($\text{BH}_{\text{max}} \sim 240 \text{ kJ/m}^3$) for high energy conversion and high operating temperatures ($T_{\text{curie}} \sim 825 \text{ }^\circ\text{C}$, $T_{\text{max.service}} \sim 300 \text{ }^\circ\text{C}$) [8]. Although NdFeB has a higher energy product ($\text{BH}_{\text{max}} \sim 400 \text{ kJ/m}^3$), it does not provide the necessary operating temperatures ($T_{\text{curie}} \sim 310 \text{ }^\circ\text{C}$, $T_{\text{max.service}} \sim 150 \text{ }^\circ\text{C}$) [8] for integration with a combustion-driven microengine, where operating temperatures may be several hundred degrees Celsius. However, it would be suitable for a low-temperature turbine generator.

Hiperco50 was selected for the rotor back iron for its combination of a reasonably high permeability ($\mu_r > 3000$) and for its high saturation flux density ($B_s \sim 2.4 \text{ T}$) to minimize the thickness of the back irons while avoiding magnetic saturation

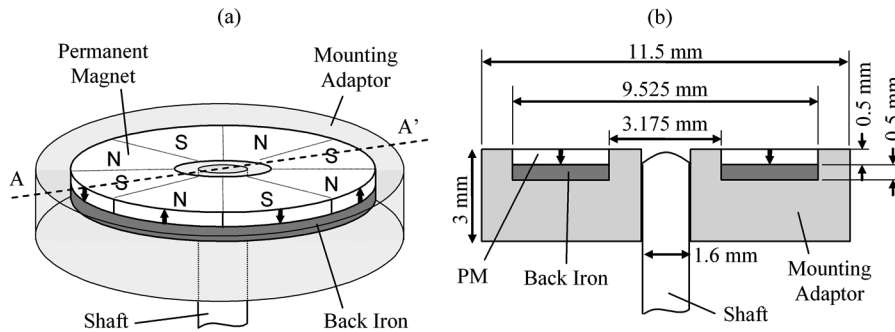


Fig. 2. Schematic. (a) Perspective view and (b) cross section of the PM machine rotors. Note that the rotor is shown upside down.

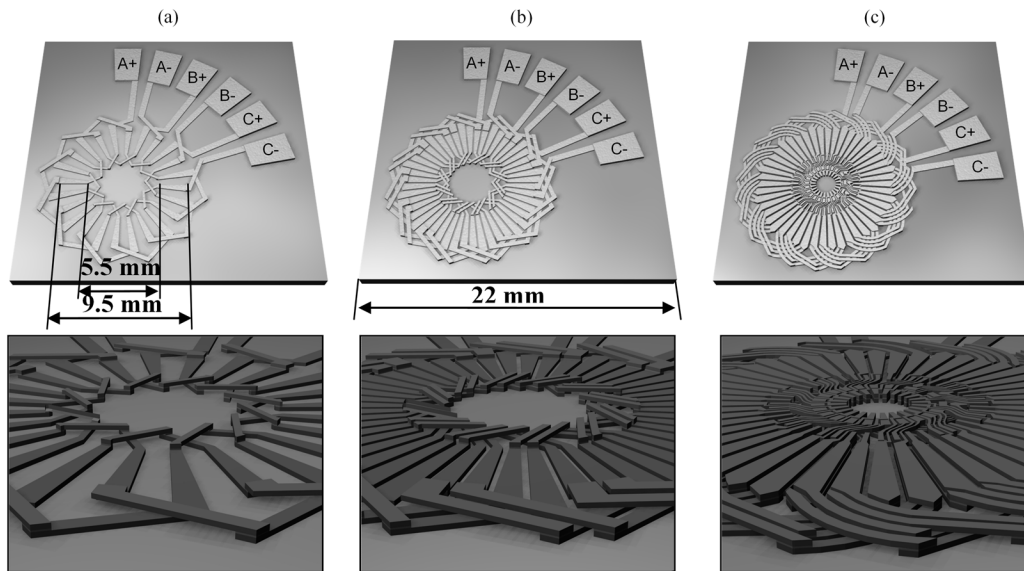


Fig. 3. Renderings of the stator winding patterns for (a) 1-turn/pole, (b) 2-turn/pole, and (c) 4-turn/pole designs.

[9]. Note that the fields in the rotor back iron are time-invariant, so the coercivity of the rotor back iron is not a major concern (no hysteresis loss).

B. Stator Design

The stator uses interleaved, three-phase, multiturn electroplated Cu windings that are dielectrically isolated from a 1-mm-thick $\text{Ni}_{80}\text{Fe}_{15}\text{Mo}_5$ (Moly Permalloy) substrate by a 3- μm spin-on-glass layer and/or 5- μm polyimide layer. The active area of the stator has an OD of 9.525 mm and an ID of 5.525 mm. Note that the ID of the stator is slightly larger than the ID of the rotor. NiFeMo is selected as the stator back iron (substrate) material for its combination of high permeability ($\mu_r > 1 \times 10^4$), low coercivity ($H_c \sim 0.16$ A/m) to minimize hysteresis losses, and commercial availability in sheets of suitable thickness [9].

The microfabricated coils, with small interconductor gaps, variable-width geometries, and complex interleaved structures, are a key enabling technology for achieving high power density in miniaturized PM generators. The winding patterns are designed for minimal resistance to ensure optimal generator performance. Increasing the number of turns results in higher induced voltages for better compatibility with the associated power electronics

(which will be discussed later). However, certain fabrication constraints (e.g., minimum feature size and highest aspect ratio) limit the geometry and overall fabrication precision.

To explore tradeoffs in output voltage/power and fabrication complexity, three different winding patterns were developed (1-, 2-, and 4-turn/pole), as shown in Figs. 3 and 4. By interleaving the coils, three distinct winding phases are possible using only two layers of metallization. The radial conductors (located directly beneath the PM rotor) are connected using appropriately arranged inner and outer end turns.

For the 1- and 2-turn/pole designs, the radial conductors reside only on the lower metallization layer, and a mesh of lower and upper level “crossovers” are used to form the end turns. In contrast, the radial conductors on the 4-turn/pole design occupy both the lower and upper metal layers and are connected by more complicated end turns. In the case of the 4-turn/pole design, the pattern is a complete double-layer winding, similar to what is used in macroscale machines [7].

For all three winding patterns, the radial conductors vary in width from 225 μm at the ID to 550 μm at the OD, with a 130- μm gap between adjacent radial conductors. The end turns of the 1- and 2-turn/pole machines have a minimum feature size of 100 μm and a minimum interconductor gap of 160 μm , while

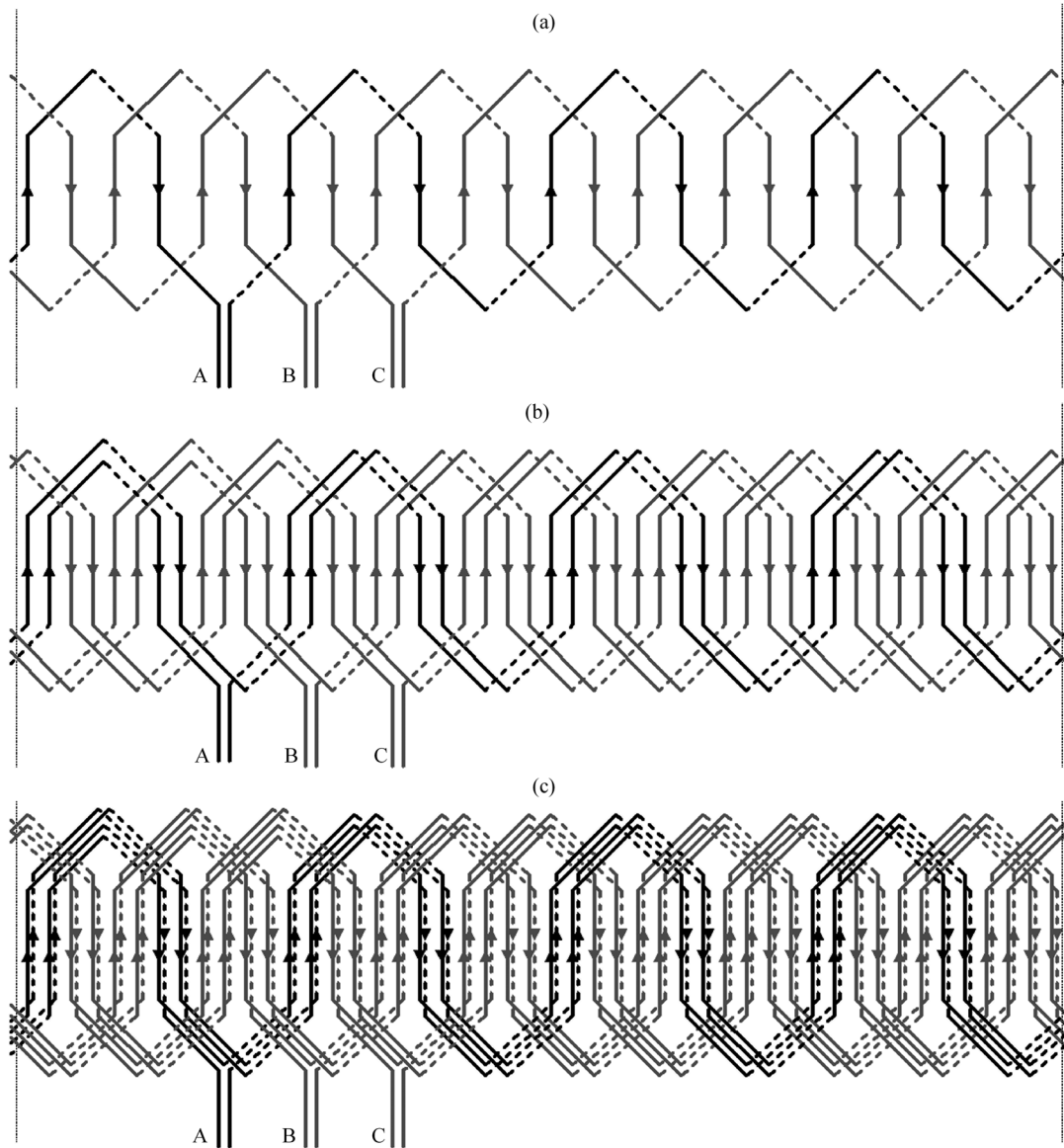


Fig. 4. Schematic winding diagrams for the (a) 1-, (b) 2-, and (c) 4-turn/pole designs. The solid line represents layer 1, and the dashed line represents layer 2. Phase A is darkened for reference.

the end turns of the 4-turn/pole machine have a minimum feature size of $40\ \mu\text{m}$ and a minimum interconductor gap of $40\ \mu\text{m}$. The number of vias is proportional to the number of turns, and the 1-, 2-, and 4-turn/pole designs use 16, 32, and 64 vias per phase, respectively.

III. DEVICE FABRICATION

The machines are fabricated using a combination of microfabrication and precision machining/assembly. Stators are microfabricated using batch-processing of multiple devices on a common substrate. In contrast, the rotor fabrication relies on precision machining and assembly. In this report, the two components are tested together for experimental characterization, but never fully integrated.

Ideally, both the stator and rotor components could both be batch manufactured and monolithically integrated. However, this requires: 1) strategies for integrating large volumes of high-quality PM materials to form the rotor using microfab-

rication processes (e.g., electroplating and spin casting) and 2) integrated high-speed bearings. Unfortunately, there are currently no reliable methods for integrating sufficient volumes of rare-earth PM materials in microfabricated systems with the precision and uniformity necessary to maintain concentricity for high-speed rotation. Furthermore, microscale high-speed bearings can be quite complex to design and fabricate. It should be noted, too, that in this design the rotor has no microscale features, so micromachining is not necessary for the rotor. Thus, the components are manufactured using appropriate micro- and macro-scale machining techniques with the near term goal of exploring high-speed, high-power-density energy conversion at small length scales. Future studies may focus on monolithic fabrication and integration.

A. Rotor

As stated previously, suitable SmCo PMs are commercially available to serve as the PM rotor. To achieve the desired

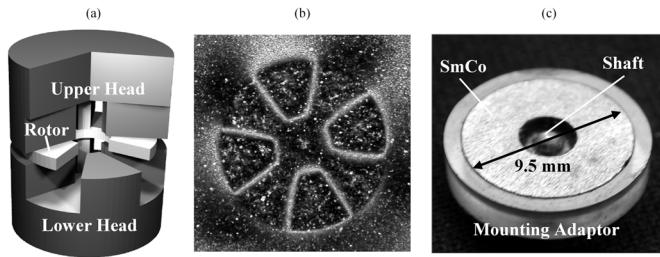


Fig. 5. (a) Cutaway view of PM rotor in magnetizing head, (b) magnetic pole pattern using magnetic viewing paper, and (c) 500- μm -thick PM rotor and back iron mounted onto shaft.

eight-pole magnetization pattern, a two-step pulse magnetization process is used. First, the rotor is uniformly magnetized in the axial direction to saturation using a high-intensity magnetic field pulse from a pulse magnetizer. Then, selected regions are magnetically reversed using a magnetizing head, machined out of $\text{Fe}_{49}\text{Co}_{49}\text{V}_2$ (Hiperco 50). As shown in Fig. 5(a), the magnetizing head has four pole pieces, which during the reversal pulse act to concentrate the fields across certain regions while shielding other regions. The areas of the PM between the head pole pieces are thus reversed due to the high magnetic fields, while the other areas experience some reversal fields due to leakage and fringing, but do not reverse.

In practice, this method requires careful selection of the magnitude of the field reversal pulse. A very small pulse will not overcome the coercivity of the already magnetized structure, resulting in little or no reversal. Conversely, a very large pulse will reverse all areas of the magnet, presumably due to leakage flux and/or saturation of the magnetizing head. These effects were not fully explored, but, instead, the magnetizing process was repeated until balanced north and south poles were achieved.

Free-field open-circuit B-field measurements are taken 250 μm above the magnet surface using a Hall-effect Gauss probe to monitor the results of the magnetization steps. After the uniform magnetization step, a B-field of $+0.06\text{ T}$ is consistently measured. After the selective reversal pulse, Hall probe measurements are used to confirm the presence of north and south poles and to evaluate their relative strength. If unbalanced, the process is repeated. For the rotor presented here, the balanced case yields equal and opposite field measurements of only $\pm 0.04\text{ T}$.

As indicated by the measurements, the B-field produced by the magnet after poling is 33% lower than the uniformly magnetized case. This could indicate that full saturation was not achieved in the rotor poles or it could be the result of inaccuracies in the field measurement. The Hall probe has a $\sim 2\text{-mm}^2$ measurement area, which is only slightly smaller than the pole itself. Also, the position and orientation of the Hall sensor within the probe casing restricts the measurements to axial-directed fields 250 μm above the magnet surface. This results in some spatial averaging and the inability to fully capture all of the leakage fields between adjacent poles (which would not be axially directed).

Regardless, the resulting eight-pole rotor magnet is shown in Fig. 5(b) using magnetic viewing paper. The rotor back iron and mounting adaptor are conventionally milled from sheets of

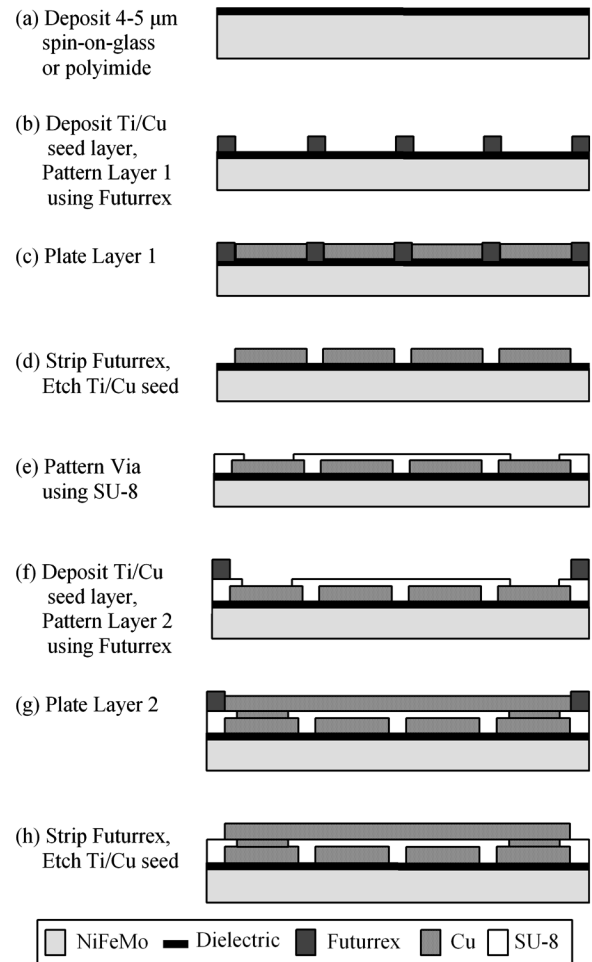


Fig. 6. Stator winding fabrication process flow.

Hiperco 50 and PMMA, respectively. The PM and rotor back iron are then glued into the mounting adaptor, which is fit onto a 1.6-mm (1/16-in) shaft for testing, as shown in Fig. 5(c).

B. Stator

The stators are fabricated using electroplated windings on 100-mm and 75-mm diameter magnetic substrates cut from 1-mm-thick sheets of $\text{Ni}_{80}\text{Fe}_{15}\text{Mo}_5$. The complete winding fabrication process flow is shown in Fig. 6. First, to isolate the coils from the substrate, a dielectric layer is deposited [see Fig. 6(a)]. Initially, a spin-on-glass (SOG) process was used, where a 1- μm PECVD SiO_2 adhesion layer was deposited, followed by $\sim 2\ \mu\text{m}$ of Accuglass T-12 SOG, and, finally, a 1- μm PECVD SiO_2 capping layer. It was later found that this layer sometimes suffered from cracking and/or pin-hole defects, resulting in shorts from the coils to the substrate, which reduced the yield. Therefore, this process is supplemented or replaced by the deposition of $\sim 5\ \mu\text{m}$ of PI-2611 polyimide.

The stator windings are constructed using a two-layer electroplating process [10], [11], identical for the three different winding patterns. First, a Ti/Cu seed layer is sputter deposited, and Futurrex NR9-8000P negative photoresist is used to pattern a $\sim 100\text{-}\mu\text{m}$ -thick mold for layer 1 [see Fig. 6(b)]. Cu is then electroplated up to the thickness of the mold [see Fig. 6(c)].

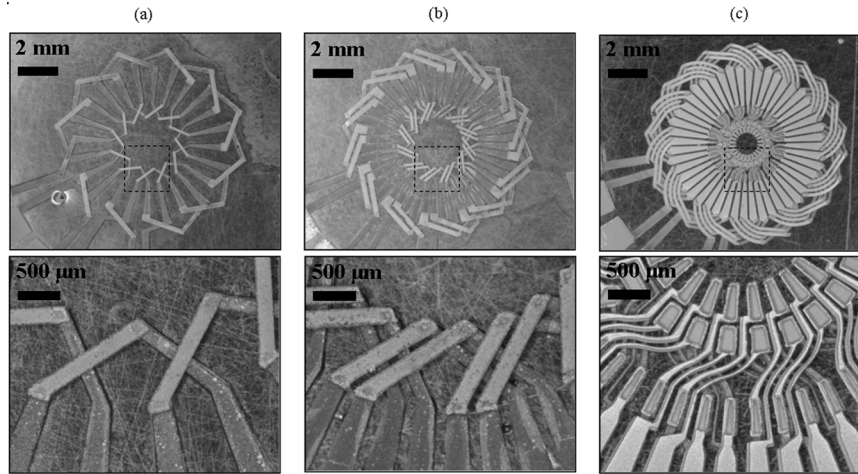


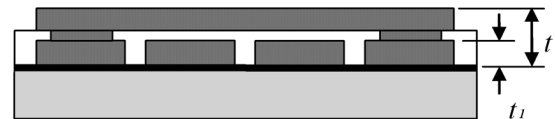
Fig. 7. Fabricated stator windings: (a) 1-turn/pole, (b) 2-turn/pole, and (c) 4-turn/pole machines.

Next, the resist is stripped using Futurrex RR4 resist remover, and the seed layers are removed by wet etching. The Cu etching uses “blue etch” (NH_4OH saturated with CuSO_4), and the Ti etching uses diluted HF acid [see Fig. 6(d)]. Then, SU-8 2025 photosensitive epoxy is used to pattern the via layer, encapsulating layer 1 except for the via openings Fig. 6(e). Then, a new Ti/Cu seed layer is sputter deposited, and layer 2 is patterned using NR9-8000P photoresist [see Fig. 6(f)]. Cu is plated to form layer 2, with the vias connecting to layer 1 [see Fig. 6(g)]. Finally, the Futurrex resist is stripped, and the seed layers are etched as before [see Fig. 6(h)]. The remaining SU-8 provides additional mechanical support, but, in the case of a high-temperature device for a microturbine, the SU-8 could be removed using oxygen-rich reactive ion etching (RIE), provided an inorganic dielectric layer was used (e.g., SOG).

Fig. 7 shows examples of the three winding patterns after fabrication. Note that, with an increasing number of turns, the patterns, particularly the inner end turns, become quite complex and, hence, more difficult to fabricate. The thicknesses of the final windings were measured optically by ablating some of the SU8 using an excimer laser system. Only the thickness of layer 1 t_1 and the total thickness t were measured, as shown in Fig. 8.

IV. SPINNING ROTOR TEST STAND

For characterization, a test stand was developed to support spinning rotors in order to demonstrate electrical power generation while avoiding the design and fabrication complexities of integrated high-speed bearings. The test stand incorporates a high-speed, air-driven spindle (High Speed Carving and Engraving Products, Federal Way, WA) to spin rotors with a controllable air gap over the surface of the stators, as depicted in Fig. 9. Powered by compressed nitrogen, the spindle provides rotational speeds in excess of 350 000 rpm. Typical operating fluidic requirements for the spindle are $1 \text{ ft}^3/\text{min}$ ($4.72 \times 10^{-4} \text{ m}^3/\text{s}$) at 45 psig (310 kPa). The rotor/shaft assembly is mounted in the spindle, and the rotation speed is measured with an optical shaft encoder or, in the case of electrical machine tests, using the frequency of the generated output.



Device	t_1	t
1-turn/pole	$\sim 125 \mu\text{m}$	$\sim 245 \mu\text{m}$
2-turn/pole	$\sim 100 \mu\text{m}$	$\sim 190 \mu\text{m}$
4-turn/pole	$\sim 80 \mu\text{m}$	$\sim 170 \mu\text{m}$

Fig. 8. Measured winding thicknesses for various PM machines.

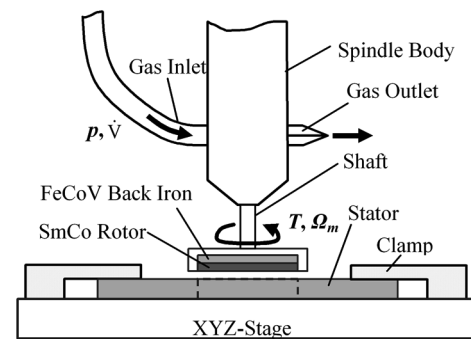


Fig. 9. Spinning rotor test stand, depicting the air-powered spindle spinning a magnetic rotor over the surface of the stator.

The shaft speed encoder is implemented by marking half of the shaft black and using a GP2L22 reflective photointerrupter (Sharp Microelectronics, Osaka, Japan). The alternating high and low reflectance creates an output signal with frequency dependent on shaft speed, which is monitored using a spectrum analyzer. This scheme minimizes the sensitivity to sensor range or position, which would cause a change in signal amplitude, but not frequency.

One challenge with the spinning rotor system is the ability to precisely position the rotor over the surface of the stator while maintaining a uniform air gap. This requires not only good registration between the rotor and stator, but also fine control over the angle between the rotor and stator. In practice, the stator is clamped to an xyz-micropositioner stage, having $\pm 5\text{-}\mu\text{m}$ resolution in all three directions. Rotors were mounted to a shaft and

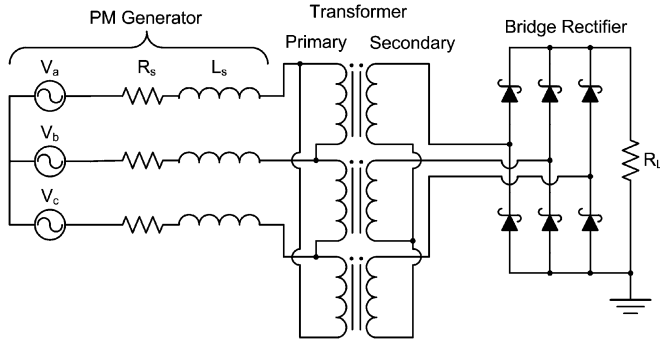


Fig. 10. Three-phase rectification circuit for dc power generation tests.

inserted into the spindle, which was attached to an articulating arm providing translation and rotation in all axes.

The alignment procedure is as follows. First, the angle between the rotor and stator is set by eye by adjusting the incident angle spindle. Then, a zero air gap is determined by bringing the stator up into contact with the rotor using the z -axis micropositioner. Due to small angular misalignments and/or irregularities in the surface of the stator or rotor, the absolute air gap is estimated to be within $\pm 25 \mu\text{m}$ of the true value. The stator is then retracted to a $250\text{-}\mu\text{m}$ gap, and the rotor is spun at a moderate speed. Alignment in the x - and y -directions is then performed by monitoring the open-circuit output voltage waveform. The position of the stator is adjusted such that a symmetric and maximal output wave is observed. Once this alignment procedure is complete, only adjustments to the air gap are made using the z -axis micropositioner control.

V. POWER ELECTRONICS

To provide power to modern electronic devices that operate using a dc voltage, the ac generator voltages are first stepped up using a three-phase Δ /wye-connected transformer ($N_1:N_2 = 1:6$ turns ratio) and then converted to dc using a three-phase diode bridge rectifier. The circuit diagram is shown in Fig. 10. The bridge rectifier uses Schottky diodes, which were selected for their small forward voltage drops ($0.3\text{--}0.4$ V). The generator windings are connected in a wye configuration and tied to the Δ -connected primary side of the transformer. This gives an additional factor of three increase from the line-to-neutral voltage of the machine (V_{oc}) to the line-to-line voltage of the transformer secondary side for an overall step-up ratio of 18, minimizing the effects of the diode voltage drops.

The generator and power electronics are modeled in PSpice to predict the output power as a function of rotational speed and load. The generator model consists of a voltage source (V_{oc}), stator resistance and inductance. An additional ~ 30 m Ω of contact resistance between the machine windings, breadboard, and transformer windings is added in series with the stator winding resistance. PSpice models for the B320A Schottky diodes were obtained from Diodes Inc.

The transformer uses three stacked EI cores (PC40EI16 from TDK), as shown in Fig. 11. The primary side consists of ten turns of 22-gauge wire in a single layer, while the secondary has 60 turns of 25-gauge wire distributed over five winding layers. The completed transformer measures approximately 40 mm long, 20 mm wide, and 10 mm thick.

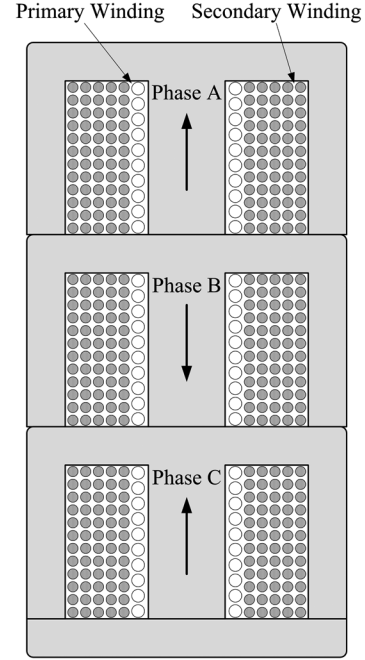


Fig. 11. Three-phase transformer core and phase windings.

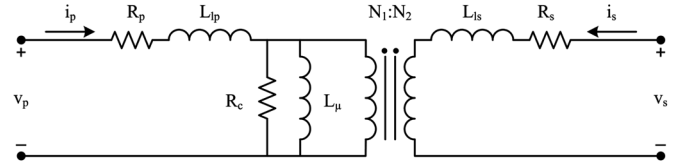


Fig. 12. Circuit model of a single phase of the transformer.

The transformer model, shown in Fig. 12, takes into account winding resistance (R_p, R_s), core resistance (R_c), leakage inductance (L_{lp}, L_{ls}), and magnetizing (L_μ) inductance. Proximity and skin effects, which increase the resistance of the transformer windings, are also taken into account [12]. The primary and secondary winding layers are converted to foils of thickness h_i , where

$$h_i = \sqrt{\frac{\pi}{4}} D_i. \quad (5)$$

The subscript i stands for either the (p)rimarily or (s)econdary winding. The porosity factor η_i for a winding layer is the total height of the coils in a layer divided by the height of the winding window l_w

$$\eta_i = \frac{N_i h_i}{l_w}. \quad (6)$$

The ratio of the effective foil thickness to skin depth Q_i is given by

$$Q_i = \sqrt{\eta_i} \frac{h_i}{\delta} \quad (7)$$

where

$$\delta = \sqrt{\frac{2}{\omega_m \mu_0 \sigma_c}}. \quad (8)$$

Defining M_i to be the number of coil layers ($M_p = 1$, $M_s = 5$), the ac resistance of the transformer windings due to proximity effect is $\kappa_{\text{proxeff},i}$ times the dc resistance R_i , where

$$\kappa_{\text{proxeff},i} = Q_i \left[\frac{\sinh(2Q_i) + \sin(2Q_i)}{\cosh(2Q_i) - \cos(2Q_i)} \right] + \frac{2(M_i^2 - 1)}{3} \left[\frac{\sinh(Q_i) - \sin(Q_i)}{\cosh(Q_i) + \cos(Q_i)} \right]. \quad (9)$$

The winding resistances, leakage inductances, and magnetizing inductances are found using an impedance analyzer. The primary and secondary resistances increase by 1.1% and 7%, respectively, over their dc values at a frequency of 6.67 kHz (corresponding to 100 000 rpm). The primary leakage is too small to accurately measure, so an approximate value is used.

The core loss in the transformer is modeled as a resistor in parallel with the magnetizing inductance [13]. In order to determine the value of its resistance, the flux density in the transformer is computed. The flux linked by the transformer core approximately equals the first harmonic of the line-to-line voltage divided by the electrical frequency

$$\lambda_{\text{core}} = N_1 A_{\text{core}} B_{\text{core}} \approx \frac{\sqrt{3} V_{\text{oc1}}}{\omega_e} \quad (10)$$

where V_{oc1} is the first harmonic of V_{oc} , N_1 is the number of primary turns, A_{core} is the area of the core, and B_{core} is the flux density in the core. Note that this is the upper bound on the core flux linkage since the voltage applied to the core will decrease as current flows through the stator windings, and a voltage drop develops across the winding resistance. Rearranging (10) and using the fact that $V_{\text{oc1}} = \lambda_{m1} \Omega_e$, B_{core} is

$$B_{\text{core}} \approx \frac{\sqrt{3} \lambda_{m1}}{N_1 A_{\text{core}}}. \quad (11)$$

Interestingly, the peak flux density in the core is independent of the speed of the generator. The core loss density is determined from core material data sheet using B_{core} . The total core loss P_{core} is simply the core loss density times the volume of the core. The core resistance is then

$$R_c = \frac{(\sqrt{3} V_{\text{oc1}})^2}{2 P_{\text{core}}} \propto \frac{f_e^2}{f_e} = f_e. \quad (12)$$

Equation (12) makes use of the fact that the core loss is approximately linear in frequency [13], so that the core resistance can be easily recomputed for power generation tests at different speeds. The results of the transformer parameter measurements and calculations are summarized in Table I using the open-circuit voltage of the 2-turn/pole machine at 100 000 rpm. The mismatch in the magnetizing inductances occurs because the “I” portions of the EI cores for phases A and B are not used.

VI. RESULTS

The stators are first characterized in terms of their phase resistance R_s , phase inductance L_s , and open-circuit voltage V_{oc} .

TABLE I
TRANSFORMER PARAMETERS

Property	Primary	Secondary
Num. turns	10	60
Wire gage	22	25
R_x @ DC	18 m Ω	225 m Ω
R_x @ 6.67 kHz	18.3 m Ω	241 m Ω
Magnetizing Inductance, L_μ	A: 56 μH B: 67 μH C: 114 μH	A: 2.0 mH B: 2.4 mH C: 4.1 mH
Leakage Inductance, L_l	A: ~ 0.01 μH B: ~ 0.01 μH C: ~ 0.01 μH	A: 16 μH B: 8.8 μH C: 17 μH
R_c @ 6.67 kHz	90 Ω	

TABLE II
LINE-TO-NEUTRAL STATOR ELECTRICAL PARAMETERS

Device	R_s (model)	R_s (measured)	L_s (model)	L_s (measured)
1-turn/pole	18 m Ω	41 m Ω	0.023 μH	0.18 μH
2-turn/pole	36 m Ω	98 m Ω	0.093 μH	0.34 μH
4-turn/pole	240 m Ω	690 m Ω	0.371 μH	1.0 μH

The machines are then connected to power electronics for power generation tests, which are conducted at varying load resistances and speeds with the rotor-stator air gap set to 100 μm .

A. Electrical Characterization

The line-to-neutral resistances and inductances (at 100 μm rotor-stator air gap) for the stators are summarized in Table II. The resistance of the 2-turn/pole machine is about twice that of the 1-turn/pole machine, which is expected since a winding in a 2-turn/pole machine is twice as long as that in a 1-turn/pole machine yet has the same cross-sectional area. The 4-turn/pole machine has a much higher resistance than that of the 2-turn/pole machine because the inner end turns have a much smaller cross-sectional area due to limited space in the center region of the machine.

The measured values are more than twice the values predicted using the resistance models in [6]. The increased resistance of the coils is attributed to the via connections between layers. The via layer is approximately 40 μm high so the thickness of the top layer coils is thinner than the difference of $t - t_1$ from Fig. 8. The contact resistance between the vias and the two coil layers also contributes a higher phase resistance. This problem gets worse as the number of vias increase with the number of turns/pole.

The phase inductance is also much larger than predicted by the analytical model. The radial span of the rotor ($R_o = 4.76$ mm, $R_i = 1.59$ mm) is used for the integration bounds to compute the flux in [6, eq. (105)]. The continuum model does not take into account the leakage inductance from the inner or outer end turns which become quite intricate as the number of turns/pole increases (Fig. 7). The leakage inductance of a macroscale machine is typically a small fraction of magnetizing inductance. In surface-wound PM machines, the leakage can be on the same order of magnitude as the magnetizing inductance. In the microscale surface-wound PM machines presented here, however, the leakage inductance actually dominates the overall stator inductance. In fact, the surface area of the outer end turns alone is 61.5 mm², which

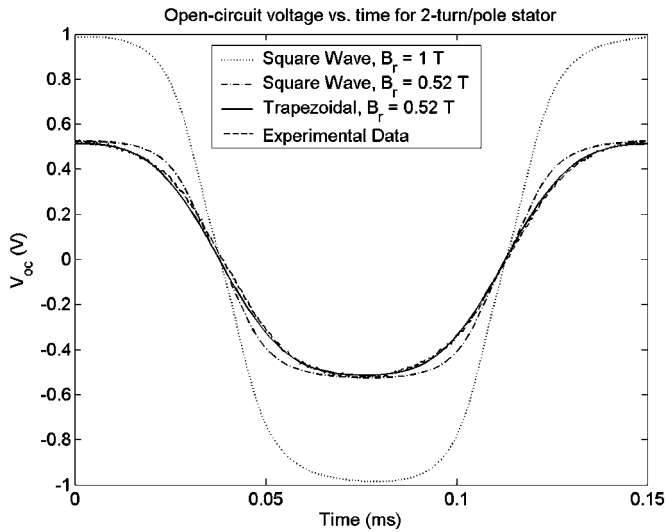


Fig. 13. Effects of smaller B_r and 1-mm transition region on open-circuit theoretical voltage waveforms [6]. Experimental data is from an eight-pole, 2-turn/pole machine at 100 krpm.

is about the same as the active area of the machine, 63 mm^2 ($R_o = 4.76 \text{ mm}$, $R_i = 1.59 \text{ mm}$).

B. Open-Circuit Voltages

The open-circuit voltage V_{oc} of each machine is measured as a function of speed with the air gap set to $100 \mu\text{m}$. A sample time waveform for the 2-turn/pole machine at a speed of 100 krpm is shown in Fig. 13, along with various theoretical curves, as predicted from the analytical model derived in [6]. The ideal square-wave magnetization with a B_r of 1 T is seen to overpredict the experimental results. The reasons for this are described as follows.

First, it is believed that the selective pulse magnetization process used to pattern the rotor may not fully saturate the material, resulting in a reduced remanence. Also, transition regions between poles are possible due to saturation of the magnetized heads at the edges of the magnetizer poles and the resulting leakage flux. This is supported by the reduced field measurements observed after magnetization, as described in Section III-A. Additional reasons for the overprediction may include nonuniform magnetic properties due to surface oxidation or stress-related damage during the manufacturing of the magnets. While these surface effects may be negligible in large-scale machines, a damaged surface layer of only $10\text{--}100 \mu\text{m}$ reduces the overall PM volume substantially in a microscale machine. One final contributing factor may be non-intimate contact between the PM and the rotor back iron, due to nonplanarity and/or surface roughness. This would increase the overall magnetic reluctance and result in a decreased field. A full investigation of these issues is not undertaken in this paper.

Despite the sources for the discrepancies, a closer fit between the analytical model and experimental results is obtained if the remanence used in the analytical model is reduced to $0.52 T$. Further improvement is made by introducing a 1-mm linear magnetization transition region [6] between the north and south

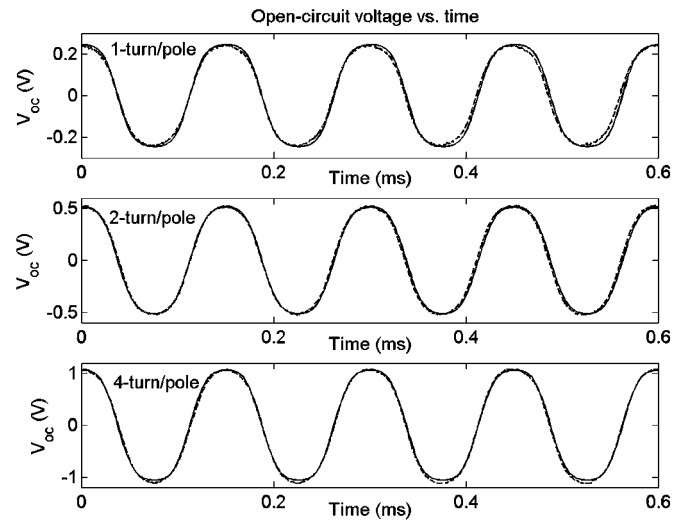


Fig. 14. Open-circuit voltage versus time for the 1-, 2-, and 4-turn/pole machines. Dotted lines represent measurement; solid lines represent the analytical model [6].

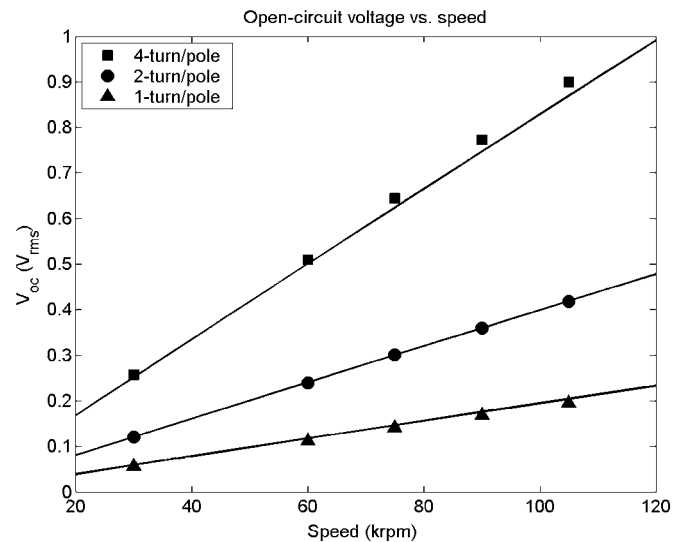


Fig. 15. Open-circuit voltages versus rotational speed for $100\text{-}\mu\text{m}$ air gap. Points represent measurements; curves represent the analytical model [6].

poles, as shown in Fig. 13. This trapezoidal profile yields a more sinusoidal shape and more likely represents the physical magnetization pattern.

Sample time waveforms for the 1-, 2-, and 4-turn/pole machines at a speed of 100 krpm are shown in Fig. 14, along with the theoretical predictions using a B_r of $0.52 T$ and a 1-mm transition region in the analytical model [6]. Note the sinusoidal shape and low harmonic content of V_{oc} , which is a result of the large air gap. Fig. 15 shows V_{oc} varying linearly with speed and number of turns per pole as expected. The open-circuit voltage is also measured as a function of air gap. Fig. 16 shows the open-circuit voltage for the same three machines at a rotor speed of 100 000 rpm. The open-circuit voltage is a decreasing function of air gap due to the exponential decay of rotor flux in the air gap.

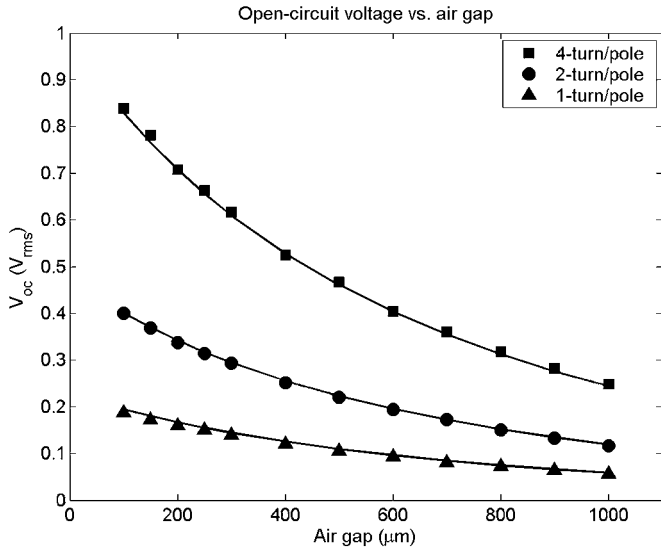


Fig. 16. Open-circuit voltages versus air gap at 100 000 rpm. Points represent measurements; curves represent the analytical model [6].

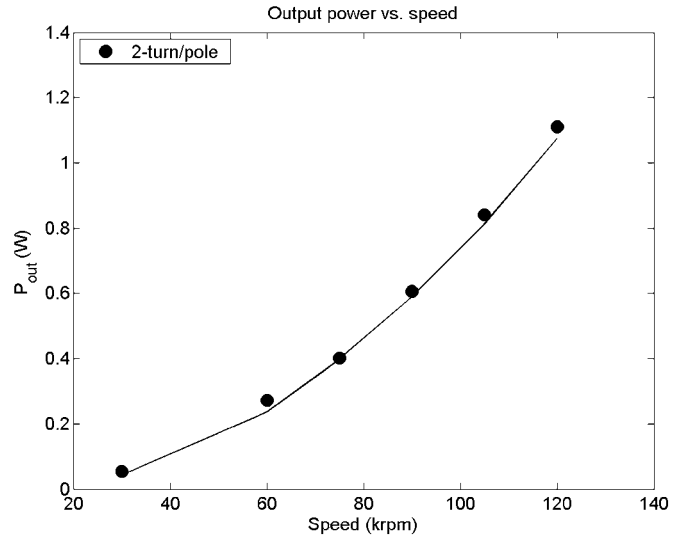


Fig. 18. DC output power across the load resistor for the 2-turn/pole machine at 100- μm air gap versus rotational speed for the 30- Ω load. Points represent measurements; curves represent the PSpice model.

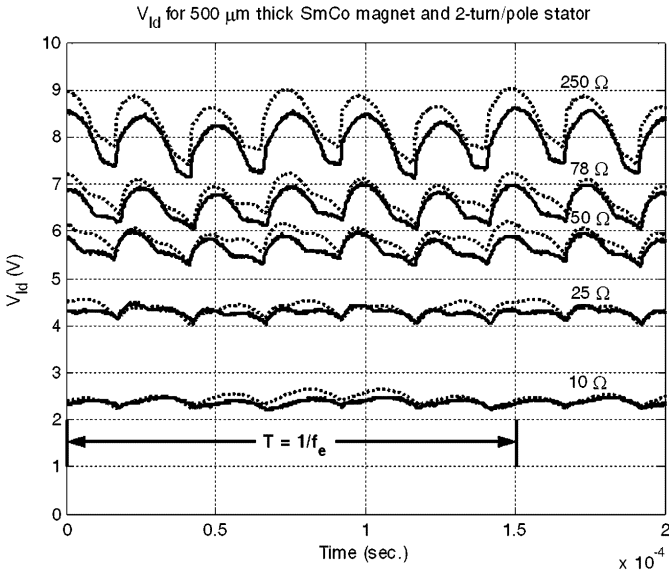


Fig. 17. Voltage across load resistor for different resistances for 2-turn/pole machine at 100- μm air gap and 100 000 rpm. Solid lines represent measurements; dashed lines represent the PSpice model.

C. DC Power Generation

Using the previously described power electronics, the rectified voltage measured across the load resistor for the 2-turn/pole machine is shown in Fig. 17 for different load resistances. The uneven ripple voltage is because the magnetizing inductances L_μ of the three-phase transformer are all different due to the core structure. This leads to different voltage divider ratios between the primary winding resistance and L_μ , producing slightly unbalanced voltages in the transformer secondary windings.

Fig. 18 plots the dc output power for the 2-turn/pole machine as a function of speed for a fixed load of 30 Ω and confirms the expected quadratic dependence on speed up to 120 000 rpm. Fig. 19 shows the dc power delivered to the load as a function of load resistance (10–250 Ω) from the 2-turn/pole machine at 80 000, 100 000, and 120 000 rpm. At the three different rotation

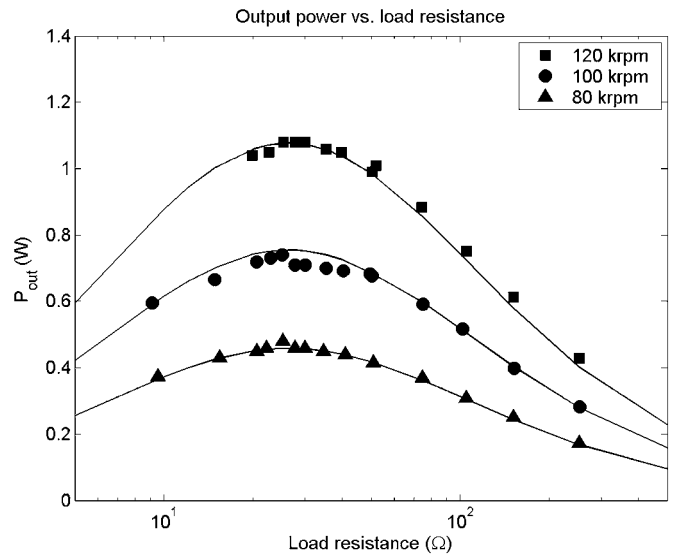


Fig. 19. DC output power across the load resistor for the 2-turn/pole machine at 100- μm air gap versus load resistance at 80, 100, and 120 krpm. Points represent measurements; curves represent the PSpice model.

speeds, the generator delivers a maximum power of 0.46, 0.76, and 1.1 W, respectively. The machine shows the expected power transfer characteristics, with output power maximized under a matched load condition of $R_l \approx 25 \Omega$. It should be noted that, though the 4-turn/pole machine produces a higher voltage than the 2-turn/pole machine does, it delivers less power because of its much larger phase resistance. All of the theoretical curves are computed using the measured values of the stator inductance, resistance, and open-circuit voltage in the PSpice model and agree well with the experimental values.

Machine efficiency is also an important consideration in the generator design. The power flow diagram for the generator is shown in Fig. 20. Direct experimental measurement of the total generator system efficiency, η_g , is challenging because of difficulty in measuring the input mechanical power P_{mech} . This

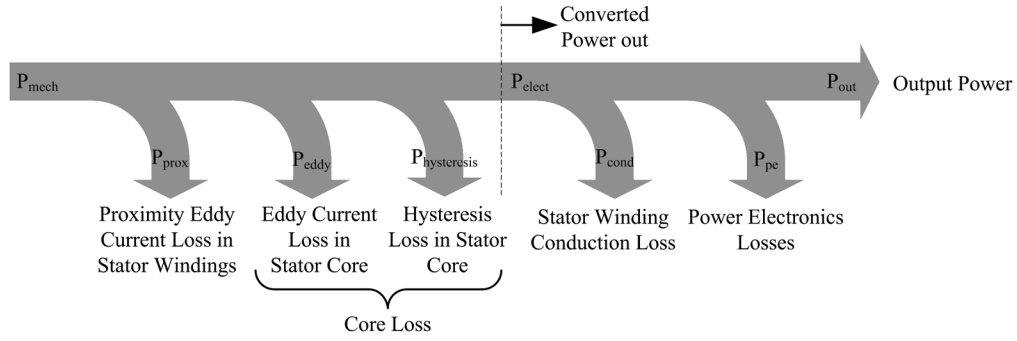


Fig. 20. Power flow diagram for PM generator system.

TABLE III
HYSTERESIS AND EDDY CURRENT LOSSES IN THE STATOR

Speed (rpm)	$P_{\text{hysteresis}}$	P_{eddy}	P_{prox}
80,000	0.097 W	1.57 W	0.047 W
100,000	0.120 W	2.24 W	0.073 W
120,000	0.144 W	3.00 W	0.104 W

input power can be determined if both the shaft speed and torque are known. Experimentally, the speed was measured using the shaft encoder, but a reliable method for directly measuring the small torque acting on the shaft was not found.

Instead, the total input mechanical power is estimated by summing the proximity loss, core loss, and converted power, $P_{\text{mech}} = P_{\text{prox}} + P_{\text{core}} + P_{\text{elect}}$. The core loss (eddy current and hysteresis losses), P_{core} , and proximity loss P_{prox} are extracted from the analytical machine model [6]. The converted power P_{elect} is power available from the open-circuit voltage in the equivalent circuit model and is extracted from the PSpice model. P_{elect} consists of stator winding conduction loss P_{cond} , power electronics losses P_{pe} , and power delivered to the load P_{out} . This approach gives a reasonable estimate for the overall efficiency of the machine but is obviously limited by the accuracy of the loss models. Other indirect methods were attempted to verify the core and proximity losses, including measurement of the temperature rise of the substrate and reciprocal power measurements using two stators. These methods gave order of magnitude confirmation of the power losses, but none provided sufficient resolution for precise verification.

Nevertheless, the core and proximity losses extracted from the device models are shown in Table III. The proximity loss is small due to the relatively slow rotational speeds (at least compared with microengine speeds), while the hysteresis loss is small because of the low coercivity of the Moly Permalloy wafer used for the stator core. The eddy current loss, on the other hand, is quite large (1.5–3 W), suggesting the need for stator laminations to minimize this loss.

Fig. 21 shows the electrical efficiency $\eta_e = P_{\text{out}}/P_{\text{elect}}$ and total generator efficiency $\eta_g = P_{\text{out}}/P_{\text{mech}}$ for the 2-turn/pole machine as functions of load resistance and speed. The efficiencies are dependent on speed due to nonlinearities in the power electronics, such as the nearly constant diode voltage drop and the nonlinear transformer core loss as a function of voltage. The generator system efficiency is substantially lower than the electrical system efficiency due to the large eddy current losses in the stator core. Because the eddy current losses are on the same order of magnitude as the output power, the stator should be

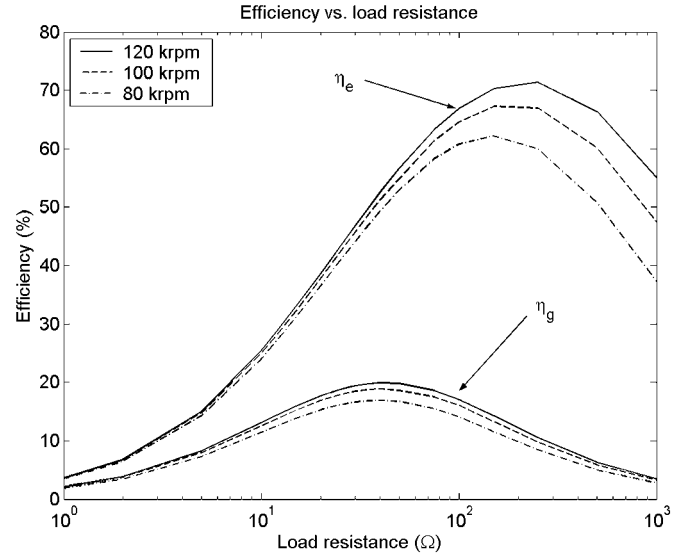


Fig. 21. Electrical system efficiency $\eta_e = P_{\text{out}}/P_{\text{elect}}$ and generator system efficiency $\eta_g = P_{\text{out}}/P_{\text{mech}}$ for a 2-turn/pole machine at 100- μm air gap.

laminated in future designs. A laminated stator would have a significantly smaller eddy current loss and achieve the best performance in terms of efficiency and output power.

At the matched load condition of $R_l \approx 25 \Omega$, the machine at 120 000 rpm shows an electrical system efficiency of 43% and a generator system efficiency of 19%. Thus, it requires 5.75 W of mechanical power, of which 2.5 W is converted by the machine to electrical power, to deliver the 1.1 W output power. The current in the stator windings when delivering 1.1 W to the load is 2.83 A_{pk} , which translates to a peak current density of $\sim 2 \times 10^8 \text{ A/m}^2$. This is one to two orders of magnitude higher than the current density found in a macroscale machine. For an active machine volume of 110 mm^3 (9.5 mm OD, 5.5 mm ID, 2.3 mm thick), the 1.1 W output power corresponds to a power density of 10 MW/m^3 .

VII. CONCLUSION

Three-phase PM generators were designed and fabricated using a combination of microfabrication and precision machining/assembly. The machines were then characterized using an air-driven spindle, and the measured open-circuit voltages were found to deviate from an ideal PM with a square-wave magnetization and 1 T remanence. The source of this discrepancy was attributed to a combination of nonidealities in PM magnetization, nonuniform PM material properties, and

nonideal contact between the PM and the rotor back iron. Nevertheless, by reducing the B_r to 0.52 T and including a 1-mm transition region between poles in the model, good agreement was achieved between the experimental and theoretical open-circuit voltages for various speeds, air gaps, and turns/pole.

The PM machines were then connected to power electronics for power generation tests. At 120 000 rpm, the 2-turn/pole machine demonstrated 2.5 W of mechanical-to-electrical power conversion and delivered 1.1 W of dc power to a resistive load. It was shown from the loss models that, at this speed, the estimated eddy current losses of 3 W in the stator core were on the same order of magnitude as the output power and therefore severely degrade overall generator system efficiency. To significantly reduce this loss and achieve higher efficiencies, future generator designs will need laminated stator cores.

The current in the stator windings when delivering 1.1 W to the load is 2.83 A_{pk} , which translates to a peak current density of $\sim 2 \times 10^8$ A/m². This is one to two orders of magnitude higher than the current density found in a macroscale machine, which is made possible by the high surface area to volume ratio of the miniaturized machine.

For an active machine volume of 110 mm³ (9.5 mm OD, 5.5 mm ID, 2.3 mm thick), the 1.1-W output power corresponds to a power density of 10 MW/m³. A typical 1000-MW turbine generator with an active volume of 60 m³ (8.4 m long, 3-m stator core outer diameter) has a power density of 17 MW/m³. The power density of the microscale PM machine is comparable to its macroscale counterpart due to its high rotation speeds and current densities. These results prove that watt-level power production is achievable using miniaturized magnetic machines and demonstrate the viability of scaled PM generators for portable power applications.

REFERENCES

- [1] D. Taghezout, "A new micromachined disc type motor," in *Proc. 7th Int. Conf. Sensors, Transducers, Syst. (Sensor '95)*, 1995, pp. 715–720.
- [2] P.-A. Gilles, J. Delamare, O. Cugat, and J.-L. Schanen, "Design of a permanent magnet planar synchronous micromotor," in *Proc. 35th Mtg. IEEE Ind. Appl. Soc.*, Oct. 2000, vol. 1, pp. 223–227.
- [3] C. Yang, "An axial flux electromagnetic micromotor," *J. Micromech. Microeng.*, vol. 11, pp. 113–117, 2001.
- [4] A. S. Holmes, G. Hong, and K. R. Buffard, "Axial-flux permanent magnet machines for micropower generation," *J. Microelectromech. Syst.*, vol. 14, no. 1, pp. 54–62, Feb. 2005.
- [5] H. Raisigel, O. Cugat, J. Delamare, O. Wiss, and H. Rostaing, "Magnetic planar micro-generator," in *Proc. Transducers'05: 13th Int. Conf. Solid-State Sensors, Actuators and Microsystems*, Seoul, Korea, pp. 757–761.
- [6] S. Das, D. P. Arnold, I. Zana, J.-W. Park, M. G. Allen, J. H. Lang, and , "Microfabricated multiwatt permanent-magnet generators—Part I: Design and modeling," *J. Microelectromech. Syst.*, vol. 15, no. 5, pp. 1330–1350, Oct. 2006.
- [7] M. S. Sarma, *Electric Machines*, 2nd ed. New York: West, 1994.
- [8] *Standard Specifications for Permanent Magnet Materials*, [Online]. Available: <http://www.intl-magnetics.org/pdfs/0100-00.pdf>
- [9] R. M. Bozorth, *Ferromagnetism*. New York: IEEE Press, 1993.
- [10] J.-W. Park and M. G. Allen, "Ultra low-profile micromachined power inductors with highly laminated Ni/Fe cores: Application to low-megahertz DC-DC converters," *IEEE Trans. Magn.*, vol. 39, no. 5, pp. 3184–3186, Sep. 2003.
- [11] M. G. Allen, "MEMS technology for the fabrication of RF components," *IEEE Trans. Magn.*, vol. 39, no. 5, pp. 3073–3078, Sep. 2003.
- [12] R. W. Erickson and D. Maksimovic, *Fundamental of Power Electronics*. Norwell, MA: Kluwer, 1999.
- [13] J. G. Kassakian, M. F. Schlecht, and G. C. Verghese, *Principles of Power Electronics*. Reading, MA: Addison-Wesley, 1991.



David P. Arnold (S'97–M'04) received B.S. degrees in electrical engineering and computer engineering and the M.S. degree in electrical engineering from the University of Florida, Gainesville, in 1999, 1999, and 2001, respectively, and the Ph.D. degree in electrical engineering from the Georgia Institute of Technology, Atlanta, in 2004.

In 2005, he joined the Department of Electrical and Computer Engineering, University of Florida, as an Assistant Professor. His research focuses on the design, fabrication, and characterization of magnetic

and electromechanical microsensors/microactuators, as well as miniaturized power and energy systems.

Dr. Arnold is a member of Eta Kappa Nu, Tau Beta Pi, and the American Society for Engineering Education.



Sauparna Das (M'03) received B.S. degrees in electrical engineering and mathematics, the M.Eng. degree in electrical engineering, and the Ph.D. degree in electrical engineering from the Massachusetts Institute of Technology (MIT), Cambridge, in 2002, 2002, and 2005, respectively. He carried out his Master's thesis at Analog Devices Inc. under a fellowship from the MIT Electrical Engineering and Computer Science Internship program designing high-frequency dc–dc converters for cell phone power applications (2001–2002). His doctoral thesis

focused on the development of magnetic machines and power electronics for Power-MEMS applications.

He is currently a Design Engineer with Linear Technology, North Chelmsford, MA, designing power management ICs for portable electronic devices. His interests include the modeling, design, and control of electromechanical systems and power electronics.

Dr. Das is a member of Eta Kappa Nu.



Jin-Woo Park received the B.S. degree in electrical engineering from Sung Kyun Kwan University, Seoul, Korea, in 1996, and the M.S. and Ph.D. degrees in electrical and computer engineering from the Georgia Institute of Technology (Georgia Tech), Atlanta, in 2000 and 2004, respectively.

After graduation, he was a Postdoctoral Fellow with Georgia Tech. Currently, he is with Cardiomems Inc, Atlanta, as a MEMS Project Engineer. His research interests include design and fabrication of wireless MEMS pressure sensors for biomedical

applications and micromachined magnetic components for compact power applications.



Iulica Zana (M'98) received the B.S. and M.S. degrees in materials science and engineering from the University "Politehnica" of Bucharest, Bucharest, Romania, in 1994 and 1995, respectively, and the Ph.D. degree in metallurgical and materials engineering from the University of Alabama, Tuscaloosa, in 2003.

From 2003 to 2004, he held a postdoctoral appointment with Prof. M. G. Allen's group at the Georgia Institute of Technology, Atlanta. He is currently a Postdoctoral Research Fellow with the

Center for Materials for Information Technology, University of Alabama. He has been working on the development and implementation of high-performance magnetic materials into new microfabricated magnetic devices. His research interests span from deposition to characterization of magnetic materials.



Jeffrey H. Lang (S'78–M'79–SM'95–F'98) received the S.B., S.M., and Ph.D. degrees from the Department of Electrical Engineering and Computer Science, Massachusetts Institute of Technology (MIT), Cambridge, in 1975, 1977, and 1980, respectively.

He joined the faculty of MIT in 1980, where he is now a Professor of Electrical Engineering and Computer Science. He served as the Associate Director of the MIT Laboratory for Electromagnetic and Electronic Systems between 1991 and 2003 and as an Associate Editor of *Sensors and Actuators* between 1991 and 1994. His research and teaching interests focus on the analysis, design, and control of electromechanical systems with an emphasis on rotating machinery, micro-scale sensors and actuators (MEMS), and flexible structures. He has written over 180 papers and holds 11 patents in the areas of electromechanics, power electronics, and applied control. He is also the coauthor of *Foundations of Analog and Digital Electronic Circuits* (Morgan Kaufman, 2005).

Prof. Lang is a former Hertz Foundation Fellow and has been awarded four best-paper prizes from IEEE societies.



Mark G. Allen (M'89–SM'95) received the B.A. degree in chemistry, the B.S.E. degree in chemical engineering, and the B.S.E. degree in electrical engineering from the University of Pennsylvania, Philadelphia, in 1984, and the S.M. and Ph.D. degrees in microelectronic materials from the Massachusetts Institute of Technology, Cambridge, in 1986 and 1989, respectively.

He joined the faculty of the Georgia Institute of Technology, Atlanta, in 1989, where he currently holds the rank of Professor and the J. M. Pettit

Professorship in Microelectronics. His research interests are in the areas of micromachining and microelectromechanical systems (MEMS), in particular the development and application of new fabrication technologies for micromachined devices and systems.

Prof. Allen was General Co-Chair of the 1996 IEEE MEMS conference and is the North American Editor of the *Journal of Micromechanics and Microengineering*.